Coherent combination of micropulse semiconductor amplifiers for water vapor differential absorption lidars

Qin Liu, Sylvie Janicot, Patrick Georges, Gaëlle Lucas-Leclin

Coherent combination of micropulse tapered amplifiers at 828 nm for direct-detection lidar applications

QIN LIU[1,*], SYLVIE JANICOT[1], PATRICK GEORGES[1], AND GAËLLE LUCAS-LECLIN[1]

[1] Université Paris-Saclay, Institut d'Optique Graduate School, CNRS, Laboratoire Charles Fabry, 91127, Palaiseau, France
[*] Corresponding author: gaelle.lucas-leclin@institutoptique.fr

Compiled December 19, 2022

We report on the design of a compact master oscillator power amplifier (MOPA) diode laser architecture at 828 nm suitable for direct-detection lidars, specifically applied to water vapor differential absorption lidars. Coherent beam combination of two pulsed high-brightness tapered amplifiers (1 µs, 10 kHz), seeded by a DBR laser diode, is demonstrated. The phase dynamics during the pulses have been thoroughly investigated. The main limitation to the CBC efficiency is quantified. The maximum combined pulse energy reaches 10.3 µJ with combining efficiency above $82\% \pm 5\%$**.**

http://dx.doi.org/10.1364/ao.XX.XXXXXX

1. INTRODUCTION

Continuous monitoring of atmospheric parameters and components is highly demanded in the atmospheric science community. Lidar is one of the key atmospheric remote-sensing techniques due to its ability to deliver high-resolution measurements[1]. Differential absorption lidars (DIAL) can provide a self-calibrated, range-resolved atmospheric components mapping with a relatively low-power laser source[2]. It requires a pulsed laser source with high spectral purity, which operates at two wavelengths – one at the absorption line and the other away from it[2]. In recent years, diode-laser-based DIAL architectures for water-vapor measurements have been constructed[3, 4], which have demonstrated long-term autonomous operations under a wide range of atmospheric conditions [4, 5]. They utilize two DBR diode lasers operating at 828.187 nm and 828.287 nm to inject one tapered semiconductor optical amplifier (TSOA) alternatively. The transmitted pulse energy reaches 5 µJ, which is limited by the maximum peak power that can be extracted from a TSOA. Though this is adequate in ground-based platforms, a higher pulse energy would be required for an airborne system to achieve a high-resolution measurement along the airplane traveling axis. The pulse energy can be further increased by combining beams from multiple emitters. Among the different beam-combining techniques that have been investigated[6], coherent beam combination (CBC), which is based on the constructive interference of coherent beams, is the only approach that preserves the spectral purity as well as the beam quality of the initial emitters[7, 8]. With careful phase control and superposition of the beams, the combined output would increase in power. Coherent combination of diode lasers has been demonstrated in continuous-wave (CW) operation with up to 47 edge-emitting ridge-waveguide amplifiers resulting in a combined power of 40 W at 1064 nm[9]. CBC of TSOAs has also been achieved in CW operation, and in pulsed regime with millisecond-long pulses[10]. A maximum CW power of 17 W was demonstrated with only 4 coherently combined TSOAs seeded by a DFB laser diode at 976 nm. In pulsed operation (2 ms - 50 Hz), the peak power could be increased up to 23 W. It is noteworthy that under pulsed operation, diode laser devices experience temperature and carrier dynamics. Therefore, the beam properties and the accumulated phase are not steady during the pulse. It makes the phase-locking and coherent superposition of the beams more challenging.

In this paper, we demonstrate for the first time the coherent beam combination under a µs-pulse regime of two TSOAs operating at 828 nm. The phase dynamics through the TSOAs during the optical pulse are investigated. The phase difference between the amplified beams is actively locked to maximize the combined pulse energy. The experimental combining efficiency is evaluated and compared to theoretical estimations to understand its limitation. Eventually, the mid-term average power stability is measured. The CBC architecture is shown as an innovative approach for the future development of high peak-power diode-laser-based pulsed sources as those required in direct-detection lidars.

2. DESCRIPTION OF EXPERIMENTAL SETUP

The MOPA architecture applied in this work is shown in figure 1. The seed laser source (MO) is a DBR laser diode (Photodigm, Inc., PH828DBR180T8) operated in CW mode with a maximal operation power of 235 mW. It has a narrow spectral linewidth ($\leq$5 MHz), as measured from the frequency noise spectral density in an integration time of 1 ms. The central wavelength is 828 nm and can reach the online and offline wavelengths of water absorption features by temperature tuning. The seed beam is collimated and optically isolated (>60 dB) to prevent power and spectral instabilities induced by optical feedback. The beam is coupled into a polarization-maintaining (PM) single-mode fiber connected to a 90:10 PM fiber coupler. The 10% output is utilized for seed power and wavelength monitoring. The 90% output is connected to a 50:50 PM fiber coupler to inject the two

power amplifiers (A_1 and A_2). The power amplifiers are commercial tapered semiconductor optical amplifier devices (TSOA, Eagleyard Photonics, EYP-TPA-0830) centered at 830 nm. They consist of a single-mode ridge-waveguide section followed by a flared section. Their output electric fields are linearly polarized, and parallel to their junction plane. Under CW operation, the maximum output power is 1.1 W at 3 A. The fiber-coupled seed beams are collimated by fiber collimators (Thorlabs, F280APC-850, L_3: f_3 = 18.45 mm) and coupled into the ridge section of the two TSOAs by aspheric lenses (L_4: f_4 = 8 mm). Each TSOA is electronically driven by a commercial current driver (PicoLAS, LDP-V 50-100) with 1 µs pulse duration, 10 kHz repetition rate, and pulse rise time of 40 ns (see figure 2). Due to the low operation duty cycle (1%), TSOAs can be overdriven to high currents beyond their specifications without thermal rollover effects.

The amplifier peak output power P_{out} follows closely the relationship $P_{out} = G_0(I) \times P_{in}/(1 + P_{in}/P_{sat})$ where $G_0(I)$ is the small-signal gain at the driving current I, P_{in} is the injection power and P_{sat} is the saturation power. P_{sat} is below 4 mW under our typical operating conditions. The input power P_{in} is chosen at about 24 mW for each TSOA in order to saturate the amplifier and maximize the output power. The maximal peak power reaches 6.7 W (corresponding to a pulse energy of 6.7 µJ) at a current of 8.1 A. The slope efficiency of the individual amplified beams remains constant at about 1.1 W/A throughout our range of driving currents. The astigmatic amplified beams are collimated in the fast axis (FA) by aspheric lenses (L_5: f_5 = 2.75 mm) and in the slow axis (SA) by cylindrical lenses (L_6: f_6 = 12.7 mm). The lens positions are carefully aligned to maximize the overlap of the amplified beams of the two TSOAs at 5.3 A. A 6-axis high-precision mounting stage is used for the alignment of all lenses before they are glued into place to obtain long-term operation stability of the laser source. The collimated beams are slightly multimode with $M^2{}_{4\sigma}$ factors $\leq 3.2 \times 1.6$ at 5.3 A.

The amplified beams are recombined using a Mach–Zehnder interferometer architecture and superposed on a non-polarizing 50:50 beamsplitter in free space. The piston phase difference varies with time due to thermal and acoustic noises both in the TSOAs and in the environment. It can be corrected by actively controlling the path difference between the two interferometer arms. The TSOAs and the CBC sections including fiber collimators, and coupling optics are mounted on a 22 cm × 18 cm × 0.6 cm aluminium breadboard which is thermally controlled by Peltier elements.

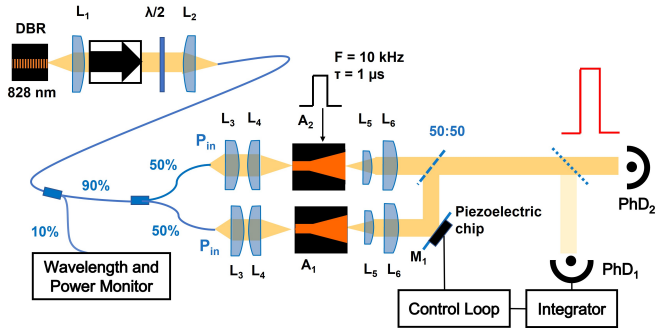

Fig. 1. Diode-laser-based source with coherent beam combination of two high brightness tapered amplifiers (A_1 and A_2).

3. EVALUATION OF SYSTEM PERFORMANCE

A. Phase dynamics during the pulse

The phase dynamics during the pulses were measured by interfering each amplified beam independently with the 10% output of the coherent seed beam. The CW seed beam was circularly polarized by a quarter wave plate, and superposed with the amplified beam on a polarizing beamsplitter. Then the in-phase signal (I) and quadrature signal (Q) are measured separately and the phase evolution $\phi(t)$ is deduced from $\arctan(Q(t)/I(t))$[11]. Figure 2 shows the resulted phase drifts experienced by the amplified beams at 2.2 A, 5.3 A, 6.9 A, and 8.1 A. The phase drift evolves almost linearly after the first 50 ns of pulse, which is attributed to the temperature evolution of the device[12]. The positive phase drift measured within the first 50 ns of the pulse could be contributed to the high-frequency current modulation at the beginning of the pulse and measurement errors due to the rapid change of pulse power. The consistency of our phase evolution measurement is validated by overlapping 20 consecutive measurements at 8.1 A. The relative phase difference, or the envelope magnitude of the overlapped data points, is in the range of 0.11 π on average. Hence, the phase drift during the pulse is repeatable from pulse to pulse. At 8.1 A, the amplitude of the phase change reaches 4.6 π.

Although the phase drift during the pulse is large in magnitude, its evolution is similar between the two TSOAs. The maximal phase drift difference is 0.17 π at ~5.3 A as shown in figure 2. To evaluate the effect of this piston phase mismatch during the pulse, the temporal power profile of coherently combined pulses $P_{CBC}(t)$, defined as

$$P_{CBC}(t) = \frac{1}{2}(P_1(t) + P_2(t) + 2\sqrt{P_1(t) \times P_2(t)} \times \cos(\phi_1(t) - \phi_2(t))) \quad (1)$$

is calculated from the individual amplified pulse profiles $P_1(t)$ and $P_2(t)$ and the phase evolutions $\phi_1(t)$ and $\phi_2(t)$ in figure 2. The CBC efficiency $\eta_{CBC} = E_{CBC}/(E_1 + E_2)$, based on the pulse energy $E_n = \int_0^{1\mu s} P_n(t)\,dt$, remains high during the pulse with an average efficiency of 98% at 5.3 A. It confirms that the phase mismatches between the two TSOAs during the 1 µs-pulses are small enough and will not deteriorate significantly the overall combining efficiency.

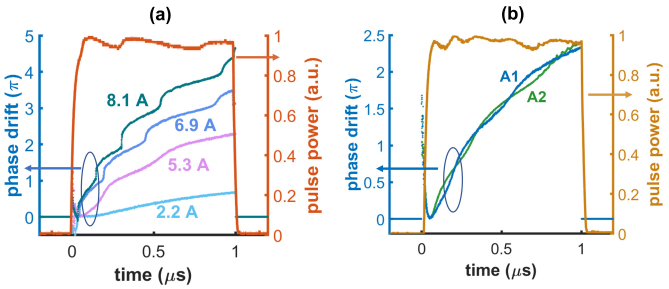

Fig. 2. a) The phase evolution during the pulse experienced by the amplified beams at 2.2 A, 5.3 A, 6.9 A, and 8.1 A with a magnitude of 0.7 π, 2.3 π, 3.5 π, and 4.6 π respectively. The pulse shape (red) is plotted for reference. b) Phase drifts experienced by the amplified pulses of A_1 and A_2 at ~5.3 A. The resulting combined pulse profile (brown) is calculated using eq.(1) from the pulse temporal profiles and phases.

B. Analysis of beam profiles

The spatial overlap of the two amplified beams on the combining element - both in intensity and phase - is the most impacting parameter on the coherent combining efficiency of two beams in a filled-aperture architecture. The local CBC efficiency $\eta_{local}(x,y)$ is given by

$$\eta_{local}(x,y) = \frac{1}{2}\frac{|\sqrt{I_1(x,y)}e^{i\phi_1(x,y)} + \sqrt{I_2(x,y)}e^{i\phi_2(x,y)}|^2}{|\sqrt{I_1(x,y)}e^{i\phi_1(x,y)}|^2 + |\sqrt{I_2(x,y)}e^{i\phi_2(x,y)}|^2} \quad (2)$$

and the overall combining efficiency η_{CBC} is computed by an intensity-weighted average of the local CBC efficiency over the whole intensity profile[8]:

$$\eta_{CBC}^{spatial} = \frac{\int\int[(I_1(x,y) + I_2(x,y)) \times \eta_{local}(x,y)]\,dxdy}{\int\int[I_1(x,y) + I_2(x,y)]\,dxdy} \quad (3)$$

The far-field intensity profiles $I_n(x,y)$ of the two amplified beams A_1 and A_2 were captured with a CMOS camera at 40 cm after the beamsplitter for an integration time of 40 ms (figure 3). These images are thus the time average measurements of a few hundred pulses. On the other hand, because of the existence of side lobes in the slow-axis profile intrinsically induced by the tapered sections, the phase distribution of the full beams $\phi_n(x,y)$ cannot be correctly deduced with a wavefront sensor. We assumed here a perfect overlap of the phase profiles ($\phi_1(x,y) = \phi_2(x,y)$). The local CBC efficiency $\eta_{local}(x,y)$ computed at the driving current of 8.1 A is shown in figure 3.c. The output powers of the two TSOAs differ by 10% since the driving current of A_2 is slightly adjusted ($\pm$ 5%) to maximize the phase drift matching at high driving currents (see section 3.A). However, the power mismatch does not affect significantly the CBC efficiency $\eta_{CBC}^{spatial}$. This value is estimated to be 94.0% which is an averaged combining efficiency rather than an instantaneous value during the pulse. The efficiency remains constant for all driving currents.

Considering both the temporal phase mismatch during pulses (see section 3.A) and the intensity overlap calculated here, we expect the experimental combining efficiency to be below 92%, as the spatial phase profile overlap was assumed perfect in our evaluation.

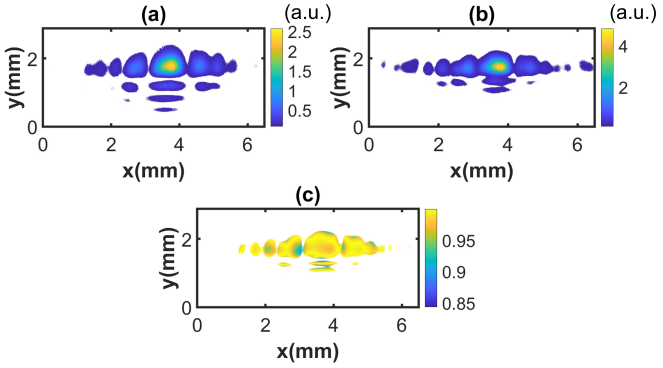

Fig. 3. Beam intensity profile of A_1 (a) and A_2 (b) and theoretical evaluation of CBC efficiency profile $\eta_{local}(x,y)$ (c) at 8.1 A.

C. Analysis of the phase stabilization operation

The synchronization of the two TSOA outputs is achieved by externally triggering the currents through the two amplifiers, with a delay below 10 ns. Since the piston phase drifts during the pulses only slightly reduce the constructive interference efficiency (figure 2), correction of the phase during pulses is not needed. However, the phase matching can not be maintained from pulse to pulse due to low-frequency phase drifts of the whole interferometer, which lead to an unstable combined average power at a time scale > 1 s. Those slow phase fluctuations are corrected with a servo-loop which actively controls the interferometer arm length of A_1. A small proportion of the combined beam is collected by the photodiode PhD_1 as an error signal and integrated by an RC circuit (cut-off frequency = 19 Hz). A hill-climbing algorithm is coded into a microcontroller whose voltage output controls the deformation of the piezoelectric transducer (PZT) attached to the folding mirror M_1 (figure 1). The servo loop takes a local measurement of the combined power and calculates the slope of the combined power change after applying a small voltage perturbation every 65 ms. Therefore, the phase mismatch is corrected by searching for the combined power maximum, which corresponds to a zero slope. The servo loop correction frequency is 5 Hz. To reduce the voltage perturbation on the combined power, we applied a latency time of 260 ms when the power maximum is reached. Since the low-frequency phase noise is dominated by thermal and acoustic noises (figure 4.c), the algorithm is sufficient to maintain phase matching and maximize the averaged combined pulse power.

The effect of phase stabilization at 6.9 A is demonstrated in figure 4 with the signals from the two photodiodes PhD_1 and PhD_2. PhD_1 measures the average combined power $P_{CBC} = E_{CBC} \times F_{rep}$, proportional to the mean energy per pulse E_{CBC}, whereas PhD_2 provides a time-resolved measurement of pulses. The combined pulse energy evolution over more than 1000 s with and without the stability control are shown in figure 4.a. The free-running system already exhibits good stability ($\sigma_{off} = 5.0\%$) due to the compactness and robustness of our architecture. The active phase stabilization further reduces the fluctuations to 0.4% for all operation currents, limited by the perturbation amplitude applied by the hill-climbing servo-loop. About 500 sets of combined pulses at 6.9 A recorded with PhD_2 are overlapped in the density plot (figure 4.b). The mean fluctuation between the measurements is 1.2% (control off 5.0%). The effect of the stabilization is further illustrated in the frequency domain with the relative intensity noise (RIN) power spectral density (PSD) of the average combined power with and without the servo-loop at 6.9 A (figure 4.c). The servo loop successfully corrects the low-frequency phase noise (< 0.5 Hz) with more than 20 dB of correction at f < 0.01 Hz. Extra perturbations at frequencies above 2 Hz are directly related to the stabilization algorithm with a peak at the correction frequency 5 Hz. However, the amplitude of the additional noises is much smaller than the environmental noises so the hill-climbing algorithm improves the system stability overall.

D. Coherent combining efficiency and pulse energy

The mean pulse energies of individual TSOAs, the mean combined pulse energies, and the corresponding combining efficiencies are measured from 2.2 A to 8.1 A (figure 5). The phase evolution during the pulses was matched by slight adjustments ($\pm$5%) of the drive current of A_2. The maximum peak power in the combined beam reaches 10.3 W (energy per pulse = 10.3 µJ) at 8.1 A with individual amplifiers contributing 6.7 W. The combined peak power, compared with the micropulse DIAL with one TSOA[4], increases by almost a factor of two at the same operating current. The beam quality of the combined beam is

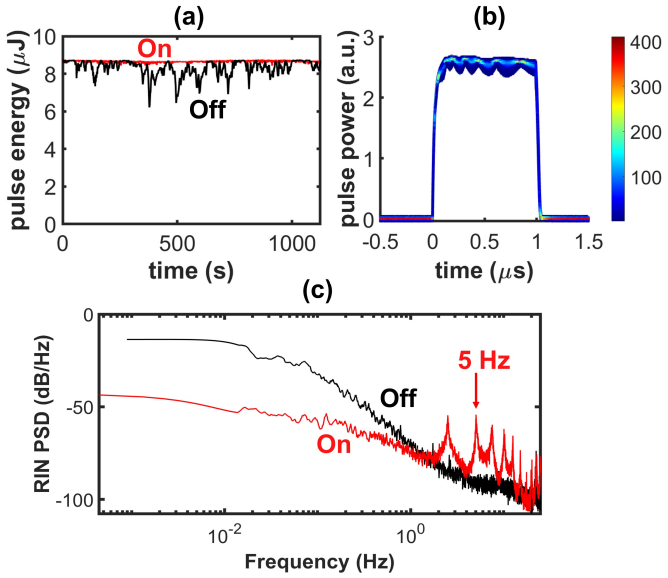

Fig. 4. a) Combined pulse energy evolution with (red) and without (black) active phase control during 1000 s of operation at 6.9 A measured by PhD_1. b) Density plot of ∼500 sets of combined pulses during 1000 s measured by PhD_2. c) Relative intensity noise PSD of the stabilized (red) and free-running (black) power measurements (PhD_1).

comparable to the one of the individual beams [10].

The combining efficiency was evaluated by different methods, such as the combined average power P_{CBC} and the pulse profiles of the combined beam $P_{CBC}(t)$. The combining efficiency decreases from 88% ± 4% at 2.2 A to 82% ± 5% at 8.1 A where the uncertainties considered the discrepancies between the different methods of efficiency evaluation. Those experimental values are lower than the estimated CBC efficiency based on the intensity profiles and residual temporal phase mismatches during pulses (92% - see section B). It could be due to slight differences in beam collimation and astigmatism correction which would impact the spatial phases $\phi_n(x, y)$ and have not been considered earlier, or a slight polarization misalignment. Therefore, although the amplifiers may not have reached their optical power limit, we did not over-drive them above 8.1 A to avoid further reduction of the system efficiency and remain within a safe range of currents below catastrophic optical damage threshold for long-term robust operation. Still, the combining efficiency is comparable to previous results with tapered devices even under different temporal regimes[7, 10].

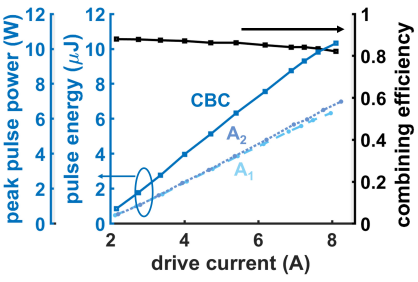

Fig. 5. Measured individual and combined pulse energies and combining efficiencies at drive currents from 2.2 A to 8.1 A.

4. CONCLUSION

In this paper, we demonstrate a compact diode-laser-based source in microsecond-pulsed operation using coherent combination of two pulsed-driven tapered amplifiers seeded by a single-frequency DBR laser diode. The phase dynamics and its impact on the combining efficiency are analyzed. The laser source reaches a peak power of 10.3 W (10.3 µJ energy per pulse) and can operate with high power stability (<0.4%) maintained by an active phase control loop. The spectral purity of the combined beam is assumed to be similar to the seed laser one, as it should not be deteriorated by the amplifiers[4] or the combining process. This laser architecture is thus fully compatible with integration in a micropulse DIAL instrument for atmospheric water vapor profiling. The performance obtained here already demonstrates the interest of coherent combining to increase the energy per pulse and improve the spatial resolution of a lidar. The CBC architecture can be adapted to different wavelengths for other direct-detection lidars. Further advancement in pulse energy can be achieved by the coherent combination of more amplifiers[10].

Funding. This project has received financial support from the CNRS through the MITI interdisciplinary programs.

Acknowledgments. We are grateful to J. Totems and P. Chazette (LSCE-UMR 1572/CEA-CNRS-UVSQ), and N. Amarouche (DT-INSU/CNRS) for fruitful discussions on the design of the DIAL system.

Disclosures. The authors declare no conflicts of interest.

Data availability. Data underlying the results presented in this paper are not publicly available at this time but may be obtained from the authors upon reasonable request.

REFERENCES

1. C. Weitkamp, *LIDAR: range-resolved optical remote sensing of the atmosphere* (Springer, New York, 2005).
2. A. R. Nehrir, K. S. Repasky, J. L. Carlsten, M. D. Obland, and J. A. Shaw, J. Atmospheric Ocean. Technol. **26**, 733–745 (2009).
3. J. L. Machol, T. Ayers, K. T. Schwenz, K. W. Koenig, R. M. Hardesty, C. J. Senff, M. A. Krainak, J. B. Abshire, H. E. Bravo, and S. P. Sandberg, Appl. Opt. **43**, 3110–3121 (2004).
4. S. M. Spuler, M. Hayman, R. A. Stillwell, J. Carnes, T. Bernatsky, and K. S. Repasky, Atmospheric Meas. Tech. **14**, 4593–4616 (2021).
5. S. M. Spuler, K. S. Repasky, B. Morley, D. Moen, M. Hayman, and A. R. Nehrir, Atmospheric Meas. Tech. **8**, 1073–1087 (2015).
6. T. Y. Fan, IEEE J. Sel. Top. Quantum Electron. **11**, 567–577 (2005).
7. G. Lucas-Leclin, P. Albrodt, D. Pabæuf, G. Schimmel, and P. Georges, "Coherent beam combining architectures for high-power laser diodes," in *Advances in High-Power Fiber and Diode Laser Engineering*, I. Divliansky, ed. (The Institution of Engineering and Technology, London, United Kingdom, 2019), p. 37–87.
8. G. D. Goodno and J. E. Rothenberg, "Engineering of coherently combined, high-power laser systems," in *Coherent Laser Beam Combining*, A. Brignon, ed. (Wiley-VCH, Weinheim, Germany, 2013), p. 3–44.
9. K. J. Creedon, S. M. Redmond, G. M. Smith, L. J. Missaggia, M. K. Connors, J. E. Kansky, T. Y. Fan, G. W. Turner, and A. Sanchez-Rubio, Opt. Lett. **37**, 5006–5008 (2012).
10. P. Albrodt, M. Niemeyer, P. Crump, J. Hamperl, F. Moron, P. Georges, and G. Lucas-Leclin, Opt. Express **27**, 27891–27901 (2019).
11. R. K. Huang, B. Chann, L. J. Missaggia, S. J. Augst, M. K. Connors, G. W. Turner, A. Sanchez-Rubio, J. P. Donnelly, J. L. Hostetler, C. Miester, and F. Dorsch, Proc. SPIE 7230,72301G (2009).
12. L. A. Coldren, S. W. Corzine, and M. L. Mašanović, *Diode Lasers and Photonic Integrated Circuits* (WILEY, New Jersey, 2012).

FULL REFERENCES

1. C. Weitkamp, *LIDAR: range-resolved optical remote sensing of the atmosphere* (Springer, New York, 2005).
2. A. R. Nehrir, K. S. Repasky, J. L. Carlsten, M. D. Obland, and J. A. Shaw, "Water vapor profiling using a widely tunable, amplified diode-laser-based differential absorption lidar (DIAL)," J. Atmospheric Ocean. Technol. **26**, 733–745 (2009).
3. J. L. Machol, T. Ayers, K. T. Schwenz, K. W. Koenig, R. M. Hardesty, C. J. Senff, M. A. Krainak, J. B. Abshire, H. E. Bravo, and S. P. Sandberg, "Preliminary measurements with an automated compact differential absorption lidar for the profiling of water vapor," Appl. Opt. **43**, 3110–3121 (2004).
4. S. M. Spuler, M. Hayman, R. A. Stillwell, J. Carnes, T. Bernatsky, and K. S. Repasky, "MicroPulse DIAL (MPD) – a diode-laser-based lidar architecture for quantitative atmospheric profiling," Atmospheric Meas. Tech. **14**, 4593–4616 (2021).
5. S. M. Spuler, K. S. Repasky, B. Morley, D. Moen, M. Hayman, and A. R. Nehrir, "Field-deployable diode-laser-based differential absorption lidar (DIAL) for profiling water vapor," Atmospheric Meas. Tech. **8**, 1073–1087 (2015).
6. T. Y. Fan, "Laser beam combining for high-power, high-radiance sources," IEEE J. Sel. Top. Quantum Electron. **11**, 567–577 (2005).
7. G. Lucas-Leclin, P. Albrodt, D. Pabæuf, G. Schimmel, and P. Georges, "Coherent beam combining architectures for high-power laser diodes," in *Advances in High-Power Fiber and Diode Laser Engineering,* I. Divliansky, ed. (The Institution of Engineering and Technology, London, United Kingdom, 2019), p. 37–87.
8. G. D. Goodno and J. E. Rothenberg, "Engineering of coherently combined, high-power laser systems," in *Coherent Laser Beam Combining,* A. Brignon, ed. (Wiley-VCH, Weinheim, Germany, 2013), p. 3–44.
9. K. J. Creedon, S. M. Redmond, G. M. Smith, L. J. Missaggia, M. K. Connors, J. E. Kansky, T. Y. Fan, G. W. Turner, and A. Sanchez-Rubio, "High efficiency coherent beam combining of semiconductor optical amplifiers," Opt. Lett. **37**, 5006–5008 (2012).
10. P. Albrodt, M. Niemeyer, P. Crump, J. Hamperl, F. Moron, P. Georges, and G. Lucas-Leclin, "Coherent beam combining of high power quasi continuous wave tapered amplifiers," Opt. Express **27**, 27891–27901 (2019).
11. R. K. Huang, B. Chann, L. J. Missaggia, S. J. Augst, M. K. Connors, G. W. Turner, A. Sanchez-Rubio, J. P. Donnelly, J. L. Hostetler, C. Miester, and F. Dorsch, "Coherent combination of slab-coupled optical waveguide lasers," Proc. SPIE 7230,72301G (2009).
12. L. A. Coldren, S. W. Corzine, and M. L. Mašanović, *Diode Lasers and Photonic Integrated Circuits* (WILEY, New Jersey, 2012).